



Cite this: *Energy Environ. Sci.*,
2016, 9, 2099

Designing thermoelectric generators for self-powered wearable electronics

Francisco Suarez, Amin Nozariasbmarz, Daryoosh Vashaee and Mehmet C. Öztürk*

Body wearable sensors and electronics for health and environment monitoring are becoming increasingly popular as their functionality increases. Thermoelectric generators (TEGs) are of interest to make these wearables self-powered by making them rely entirely on the heat harvested from the human body. The challenge with using thermoelectrics on the human body is the large thermal resistances experienced at the skin/TEG and TEG/ambient interfaces. These parasitics can be potentially so large that they can dominate the device performance. Therefore, it is critical to have accurate models to predict the device performance considering material properties, module design and parasitics. In this paper, we present a computationally efficient, quasi three-dimensional TEG model and use this model to explore the design criteria for current state-of-the-art rigid TEG modules as well as prospective flexible modules for body wearable applications. We show the impact of the properties of the thermoelectric material, module design and dimensions, heat spreaders, filler material, heat sink and skin contact resistance on device performance. We also identify the significance of material thermal conductivity over the Seebeck coefficient and electrical resistivity in improving the output power for wearable applications. For flexible TEGs, we identify the thermal conductivity of the filler material as one of the critical parameters that need to be taken into consideration for optimal performance. Finally, the model was used to design a custom TEG with improved material properties and device design. The measurements indicate a nearly 3× improvement in power output over a commercial TEG with similar area as successfully predicted by the calculations.

Received 14th February 2016,
Accepted 13th April 2016

DOI: 10.1039/c6ee00456c

www.rsc.org/ees

Broader context

The human body is an endless source of renewable energy. Useable energy in the form of heat is radiated continuously from the skin as the body self regulates a precise core temperature. Thermoelectric Generators (TEGs) are solid state (no moving parts) devices that are capable of converting heat into electrical energy. TEGs operate on the principal that when subjected to a temperature differential, they produce an associated voltage due to the Seebeck effect. Wearable devices pose as an interesting application for TEGs as the human skin and the ambient provide a natural temperature differential from which energy can be harvested. As their functionality increases, wearable devices for fitness and wellness monitoring are becoming more popular than ever before. The interest in applying these devices to applications that require long-term continuous monitoring (e.g. clinical studies) is also growing. However, the burden of frequent recharging or replacing of the batteries on these devices plagues user compliance and is currently one of the largest challenges facing the industry. By taking advantage of the available temperature difference between the body and the ambient, the wearable devices have the opportunity to not only harvest energy for improving battery life but also completely eliminate the battery all together and become truly "self-powered".

1 Introduction

Thermoelectric generators (TEGs) present a unique opportunity to convert heat radiated from the human body to electricity for self-powered wearables. The TEG technology has already been exploited in several commercial devices starting with the Seiko Thermanic watch.¹ The topic has also attracted the interest of

different research groups and it has become the focus of a number of scientific publications.^{2–6} These studies have shown that TEGs can produce hundreds of μW of power, which has proven to be sufficient for powering different body sensors such as electrocardiogram (ECG) and pulse oximeter.^{7,8} However, comprehensive modeling of how individual material dimensions, material properties, parasitic resistances, filler thermal conductivity as well as heat spreading internal and external to the device has not been performed to evaluate full system performance. There is a growing interest in using TEGs to

Department of Electrical and Computer Engineering, North Carolina State University, Campus Box 7920, Raleigh, NC 27695, USA. E-mail: mco@ncsu.edu

create self-powered wearables with increased capability to monitor the human health and the environment.⁹ Such devices will require multi-modal sensing to achieve a truly comprehensive assessment of the human condition. To achieve such a goal, TEGs must be able to deliver milliwatts of power *via* improvements in material properties and system design. The latter is especially important given the high thermal parasitic resistances at the body/TEG and TEG/air interfaces. In this paper, we present a computationally efficient quasi three dimensional model which was employed to study the impact of all key design parameters on harvesting energy from the human body. Additionally, we experimentally evaluate the output power of a commercial TEG placed on the human body and study the potential impact that a proper design could have on improving performance.

1.1 Human body as a heat source

The human body produces heat as a byproduct of metabolic chemical reactions.¹⁰ Both the conversion of organic matter into energy and the transformation of that energy into useful work contributes to our core body temperature. The heat is then distributed to different parts of the body by the blood flow and is released through the skin *via* radiation, convection and sweat evaporation.¹¹ As the ambient temperature changes, the body regulates the blood flow through contracting (vasoconstriction) and dilation (vasodilation) of the blood vessels.¹²

The skin temperature is an important factor that needs to be taken into account in choosing the optimal locations for energy harvesting. The skin temperature is naturally higher at body locations where the blood vessels are closer to the skin surface. Systematic studies that focus on measurements of the body temperature at different locations have been previously conducted. For example, Fig. 1 shows skin temperatures for various body locations reported by Webb.¹³

It can be seen that the highest temperatures are measured on the forehead and the temperatures progressively drop toward the feet. It is interesting to note however that the temperature range becomes far more significant as the ambient temperature drops. For instance, while the temperature difference, $T_{\max} - T_{\min}$ is only about 1 °C at an ambient temperature

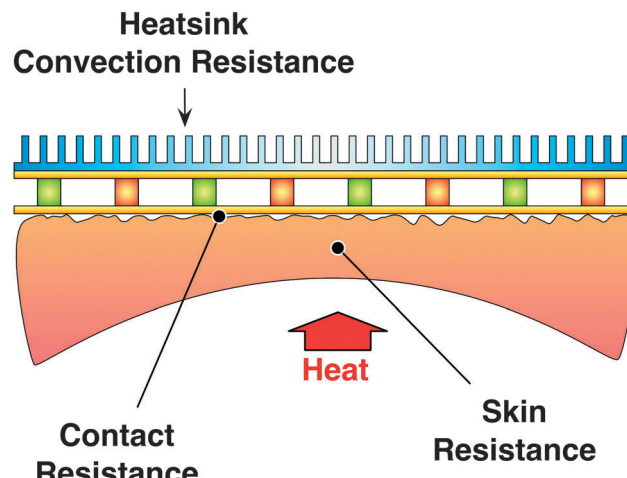


Fig. 2 Cartoon illustrating the three parasitic resistances that impact TEG performance.

of 47 °C, it increases to 8.5 °C when the ambient temperature drops to 15 °C. The standard deviation obtained for these measurements also varies with location and the ambient temperature reaching a maximum of 2 °C at 15 °C.

1.2 TEGs for harvesting heat from the human body

When a TEG is placed on the human body, the extrinsic temperature differential, ΔT_e between the body core and the ambient results in a steady flow of heat through the TEG, which leads to an intrinsic temperature differential, ΔT_i across the TEG, which in turn produces an output voltage, V_o *via* the Seebeck effect. Successful harvesting of heat from the human body relies on maximizing this temperature differential, which turns out to be a challenging task due to several parasitic thermal resistances.

Fig. 2 illustrates three key resistances that impact the efficiency of these devices. First and foremost, human skin is a good thermal insulator, which leads to a skin thermal resistance between the body core and the TEG. Second, a large thermal contact resistance exists at the skin-TEG interface due to the rough morphology of the skin. Finally, a thermal resistance exists at the TEG-ambient interface largely determined by convection. Typically, a heatsink is used to increase the convection efficiency by increasing the available surface area. However, if this device is to be used on the human body, it is quite undesirable to have a large, clunky heatsink on the TEG. Therefore, it is favorable not to use a heat sink or to use a heatsink with a small form-factor while achieving an acceptable heatsink resistance, R_{HS} at this interface. A sizable portion of the available temperature differential drops across these three resistances. Consequently, for efficient harvesting of the body heat, it becomes critical to minimize these parasitic resistances and choose the TEG parameters accordingly.

2 TEG model

In this work, a quasi three-dimensional thermal model was employed, which takes into account the lateral spread of heat

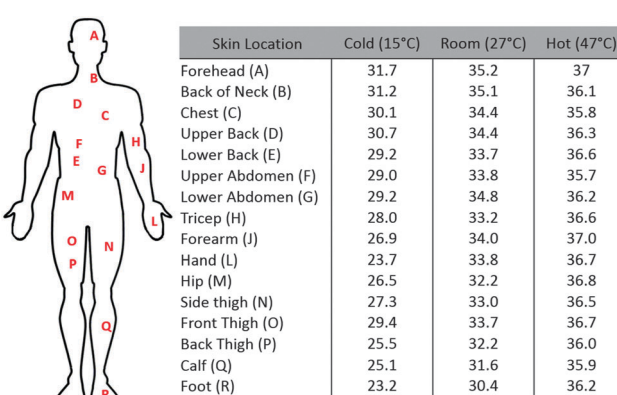


Fig. 1 Reported human skin temperatures for different points on the body at varying ambient temperatures.¹³

through the hot and cold side substrates as well as conduction through the medium surrounding the semiconductor (thermoelectric) material more commonly referred to as legs. The objective is to provide a simple model that can provide similar design insight as more sophisticated finite element analysis tools with increased flexibility for changing the geometrical parameters while providing results at a fraction of the computation time. In this section, we present the basic structure of the thermal model as well as the second order effects as incorporated in our calculations.

2.1 Basic circuit

Fig. 3 shows the electrical circuit of the basic model. In this circuit, the ambient and the core body temperatures are represented by the ideal voltage sources, T_a and T_b respectively, which define the extrinsic temperature differential as $\Delta T_e = T_b - T_a$. The intrinsic temperature differential is given by $\Delta T_i = T_h - T_c$, where T_h and T_c represent the temperatures on hot and cold sides of the thermoelectric legs respectively. The model calculates ΔT_i for a given ΔT_e and uses this differential to calculate the power generated by the thermoelectric module.

The circuit includes the thermal resistance of the legs, R_{TEG} and the three parasitic resistances illustrated in Fig. 2: the hot-side resistance, R_h , includes the skin resistance, the skin/TEG contact resistance, as well as the vertical resistance through the substrate to the leg. The cold-side resistance, R_c is mainly determined by the heatsink resistance, R_{HS} and vertical resistance through the substrate.

The two current sources $Q_j/2$ represent Joule heating resulting from the electrical current, I , flowing through the legs once the generator is connected to an external load. The net heat generated due to this current is $Q_j = I^2 R$, where R is the total electrical resistance of the TEG legs. It is assumed that this additional heat is evenly distributed between the two sides of the module. The electrical resistance of each TEG leg is determined by the electrical resistivity, ρ of the material and the physical dimensions. The net effect of this self-heating is to reduce the ΔT_i .

The two voltage dependent current sources Q_p represent Peltier heating and cooling also resulting from the electrical current flowing through the TEG. The Peltier heat pumped to or from a junction can be calculated as $Q_p = I\pi$, where I is the electric current flowing through the junction and π is the Peltier coefficient of the semiconductor. The Seebeck coefficient, α and the junction temperature, T_c or T_h determine the Peltier coefficient as $\pi = \alpha T$. It can be seen from the circuit that these sources attempt to cool the hot side and heat the cold side, effectively reducing the ΔT_i .

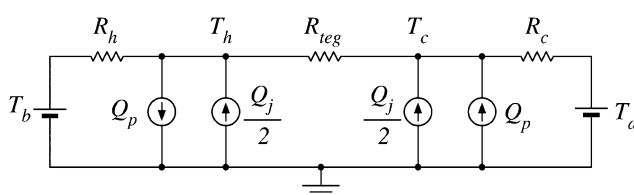


Fig. 3 Electrical analog of the thermal equivalent circuit employed by the model.

Analysis of the circuit shown in Fig. 3 yields the following equations:

$$\frac{T_h - T_c}{R_{TEG}} = \frac{T_b - T_h}{R_h} + \frac{Q_j}{2} - Q_p \quad (1)$$

$$\frac{T_h - T_c}{R_{TEG}} = \frac{T_c - T_a}{R_c} - \frac{Q_j}{2} + Q_p,$$

which can be solved simultaneously to determine $\Delta T_i = T_h - T_c$. The open-circuit voltage, V_{oc} produced by the TEG is given by

$$V_{oc} = N(\alpha_n + \alpha_p)\Delta T_i \quad (2)$$

for a TEG with N pairs of p-n legs. In this equation, α_n and α_p represent the Seebeck coefficients of the n-type and p-type legs respectively. The source resistance, R_s of the TEG is given by

$$R_s = \frac{N}{2}(\rho_p + \rho_n) \frac{h}{w^2} + R_{ext} \quad (3)$$

where h and w represent the height and width of each leg and ρ_n and ρ_p represent the electrical resistivities of the n-type and p-type legs respectively. R_{ext} includes the contact resistances at the metal-semiconductor interfaces as well as the series resistance of the metal lines connecting the TEG legs in series.

The generated open-circuit voltage is shared between the source resistance R_s and the external load resistance R_L . The power delivered to the load can then be calculated as:

$$P_{max} = \frac{V_{oc}^2}{R_s(1 + R_L/R_s)^2} \quad (4)$$

2.2 Heat flow around the legs

Since the TEG legs are attached to a thermally conductive substrate, the heat entering the bottom substrate from areas surrounding the legs also contribute to the output power generated by the TEG. However, this heat must first flow laterally through the bottom substrate before it can be collected by the TEG legs. Similarly, the heat leaving the legs spreads laterally in the top substrate before it is dissipated to the ambient through the heatsink *via* convection. The thermal resistances presented to these lateral heat flows could be negligibly small if a TEG employs relatively thick substrates made of a good thermal conductor. However, as the TEG dimensions are downscaled for wearables and flexible devices, this parasitic effect can play a significant role and it must be taken into account in the calculations.

Furthermore, some of the heat traveling through the bottom substrate escapes into the medium (typically air) surrounding the legs effectively resulting in a thermal shunt between the two substrates. For conventional TEGs, this effect can be fairly small since air is not a good conductor of heat ($\kappa \approx 0.025 \text{ W m}^{-1} \text{ K}^{-1}$ at 300 K). On the other hand, in flexible TEGs, the medium surrounding the legs is typically an elastomer, which can be far more conductive than air and it can cause a significant drop in device performance.

In our model, the lateral heat flow through the substrates and thermal shunting of the legs are treated numerically following a quasi three-dimensional approach. An electrical

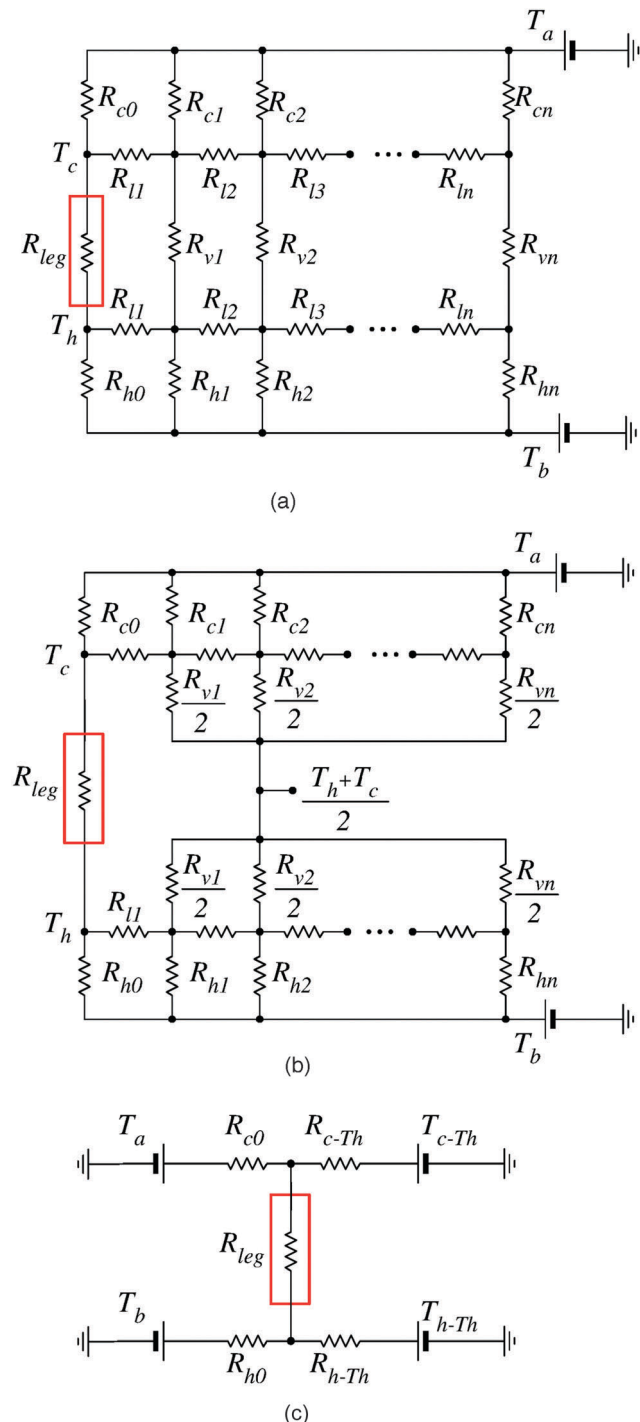


Fig. 4 (a) Complete circuit representing the heat flow around a single TEG leg; (b) circuit after separation of the hot and cold sides; (c) final circuit per leg with Thevenin equivalents.

analog circuit is created to represent the lateral, in-plane heat flow through the substrates as well as the out-of-plane flow between them. The circuit shown in Fig. 4a represents the heat flow through and around a single leg. In this circuit, R_{leg} is the thermal resistance of the leg. The resistances, R_{ho} and R_{co} represent the thermal resistances connecting the leg to the skin on the hot side and to the ambient on the cold side.

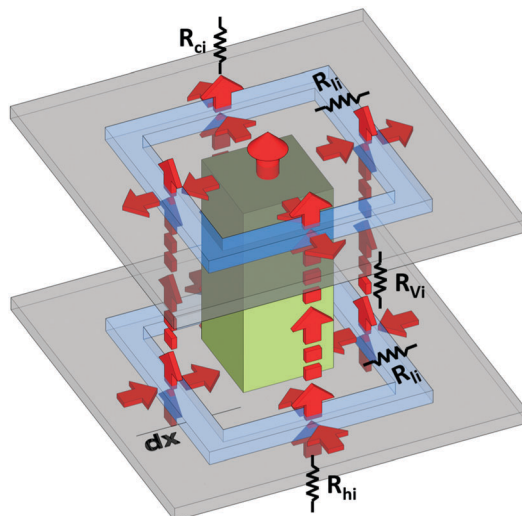


Fig. 5 3-D representation of thermal resistances around a single leg. Lateral thermal resistance, R_{li} , represents heat flow through the substrate around the legs. Vertical resistance, R_{vi} , represents vertical heat flow around the legs through the medium between the hot and cold substrates. Hot and cold side resistances R_{hi} and R_{ci} represent both the heat transfer from the heat source (body) as well as vertical conduction through the hot substrate as well as vertical conduction through the cold substrate and heat transfer to the cold source (ambient) respectively.

Fig. 5 illustrates the origin of the additional resistances included in the resistive network of Fig. 4a. The rectangular region surrounding each leg is divided into n rings of thickness, dx , which are used to calculate the in-plane and out-of-plane heat flow.

On the lower, hot-side substrate, each ring introduces two thermal resistances: a skin-to-leg resistance, R_{hi} as well as a thermal resistance, R_{li} representing the lateral flow of heat from the i th ring toward the leg, where $i = 1, 2, \dots, n$. Similarly, each ring on the top, cold-side substrate introduces three resistances: a leg-to-ambient resistance, R_{ci} largely determined by the rate of convection on this surface, a lateral resistance R_{li} representing the heat flow from the leg to the i th ring, and a vertical resistance through the filler material between the hot and cold substrates, R_{vi} .

The lateral resistance, R_{li} is determined by the thermal conductivity of the substrate and the physical dimensions: the circumference of the ring, the thickness of the substrate and the width, dx . The model assumes that the two substrates are made of the same material and that they have the same thickness. As such, the lateral resistances, R_{li} of the rectangular rings are assumed to be identical for both substrates.

To account for the heat flow between the two substrates, each ring on the bottom substrate is connected to an identical ring on the top substrate through a vertical resistance, R_{vi} . Conduction through the filler material is assumed as the dominant heat transfer mechanism.

To simplify the solution, each resistive network was represented by a Thevenin equivalent circuit. In this approach, one can reduce a large circuit consisting of voltage sources and resistors down to a simple equivalent circuit with a single voltage source in series with a single resistor.¹⁴ It was assumed that the air

temperature midway between the two substrates was fixed at $T' = (T_h + T_c)/2$, enabling separation of the upper and lower resistive networks as shown in Fig. 4b. It was then possible to obtain the Thevenin equivalent circuits for heat spreading around the legs for both sides resulting in the equivalent circuit shown in Fig. 4c where heat flow across the leg is the combination of heat flow directly underneath the leg as well as the heat collected around the leg. This circuit was then replicated for all legs in the TEG module assuming uniform heat distribution throughout the module. This implies that the same temperatures appear on hot and cold sides of every single leg yielding virtual shorts between equivalent nodes of the resistive networks representing the individual legs. These virtual shorts effectively place all TEG legs as well as the equivalent resistances in parallel yielding two final Thevenin circuits representing the entire module. These circuits were then used to replace T_a , T_b , R_c and R_h in the circuit of Fig. 3 as

$$T_a' = \frac{R_{co}' T_{c-Th} + R_{c-Th}' T_a}{R_{co}' + R_{c-Th}'} \quad (5)$$

$$T_b' = \frac{R_{ho}' T_{h-Th} + R_{h-Th}' T_b}{R_{ho}' + R_{h-Th}'} \quad (6)$$

$$R_c' = \frac{R_{ho}' \times R_{h-Th}'}{R_{ho}' + R_{h-Th}'} \quad (7)$$

$$R_h' = \frac{R_{ho}' \times R_{h-Th}'}{R_{ho}' + R_{h-Th}'} \quad (8)$$

where $R_{co}' = R_{co}/2N$, $R_{ho}' = R_{ho}/2N$, $R_{c-Th}' = R_{c-Th}/2N$, $R_{h-Th}' = R_{h-Th}/2N$.

2.3 Skin to TEG resistance

A TEG placed on the human skin sees two main resistances between the skin temperature and core body temperature as shown in Fig. 2. The first resistance is the skin resistance which is a complicated function of specific physiological parameters such as weight, age, body fat and even gender.¹² The second resistance is the thermal contact resistance at the TEG-skin interface. Since the skin is an inherently rough surface, this resistance can have a significant impact on the TEG performance. However, since skin is soft and can deform with pressure, the contact resistance at the skin/TEG interface is highly dependent on pressure.

The contact resistance, R_c between two dissimilar surfaces can be expressed in terms of the heat transfer coefficient, h_c as $R_c = 1/h_c A$ where A is the contact area. Ho *et al.* used a previous model by Yovanovich *et al.*¹⁵ to calculate the contact resistance between the fingertip and different surfaces.¹⁶ According to this model, the heat transfer coefficient at the TEG/skin interface can be expressed as

$$h_c = 1.25\kappa_s \frac{\Delta a}{\sigma} \left(\frac{P}{H_C} \right)^{0.95} \quad (9)$$

where κ_s is the harmonic mean thermal conductivity, Δa is the average surface asperity slope, σ is the RMS surface roughness

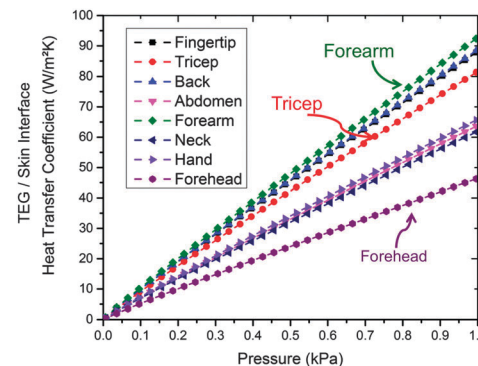


Fig. 6 Heat transfer coefficient of the TEG/skin interface as a function of pressure for various locations on the body. Common areas investigated for wearables such as the Tricep, Forearm and Forehead are highlighted. It can be seen that since the skin is soft and elastic, the contact resistance is a function of the pressure applied.

and P is the applied pressure and H_C is the micro-hardness of the skin. Fig. 6 shows the estimated heat transfer coefficient for different locations on the body as a function of contact pressure varying from 0 to 1 kPa. For reference, 0.5 and 0.8 kPa corresponds to tight fitting clothing.¹⁷ In these calculations, we have used the RMS skin roughness figures reported by Tchvialeva *et al.*,¹⁸ who used a laser speckle technique for *in vivo* measurements. For skin Δa and H_C , we have relied on values used by Ho *et al.*¹⁶ For the TEG, $\sigma_{TEG} = 1 \mu\text{m}$ and $\Delta a = 0.2 \mu\text{m}$ were assumed, which are representative of a surface much smoother than the skin. It can be seen that the heat transfer coefficient varies appreciably with pressure and shows significant variations between different locations on the body. The largest h_c (*i.e.* the smallest contact resistivity) was obtained for the forearm, which exhibits a range of 50 to 75 W m⁻² K⁻¹ for tight fitting clothing. Tricep, which exhibits a similar h_c appears to be another good location. According to these calculations, the forehead has the smallest heat transfer coefficient, corresponding to an approximate range of 25 to 40 W m⁻² K⁻¹ despite providing the highest temperature on the body according to Fig. 1.

Using the skin temperatures given in Fig. 1 for different body locations, and assuming a uniform convective heat transfer coefficient of $h_{conv} \approx 5 \text{ W m}^{-2} \text{ K}^{-1}$ ¹⁹ for the body, we can estimate the skin heat transfer coefficient, h_{skin} from

$$h_{skin} = h_{conv} \cdot \frac{T_{skin} - T_{ambient}}{T_{core} - T_{skin}} \quad (10)$$

This yields $\approx 15 \text{ W m}^{-2} \text{ K}^{-1}$ for the wrist at room temperature, which, appears to be a favorite location for commercial wearables. Clearly, this value is smaller than the heat transfer coefficients given in Fig. 6 especially with tight fitting clothing. Since the two resistances are in series, the effective heat transfer coefficient is given by

$$h_{eff} = \frac{h_c h_{skin}}{h_c + h_{skin}} \quad (11)$$

which, will be dominated by the smaller of the two coefficients. In our calculations, we have bypassed the skin resistance by

relying on average wrist skin temperatures given by assuming that this resistance is embedded in the skin temperature measured on the body.²⁰ We have then used a conservative estimate for the heat transfer coefficient of $50 \text{ W m}^{-2} \text{ K}^{-1}$ to represent the interface, which falls within the lower range of $20\text{--}100 \text{ W m}^{-2} \text{ K}^{-1}$ for the skin heat transfer coefficient reported by Lossec *et al.*⁵

2.4 Heat rejection at cold side

For the TEG to achieve a large ΔT , the ability to reject heat from the cold-side is just as important as the skin temperature. Typically, a heat sink is attached to the cold-side of a TEG to provide a large surface area for effective convective cooling. Unfortunately, heat dissipation will inevitably decrease if the TEG (and the heat sink) are buried under clothing. Therefore, potential usable locations include the neck, face, arms and possibly the lower legs. Furthermore, forced convection relies on air flow and since air flow increases with body motion, locations that are naturally more mobile (*e.g.* arms and legs) will be advantageous.²¹

The heat sinks used on wearable devices must be efficient yet non-burdening. This simply means that we should try our best to avoid large, bulky heat sinks. This requirement unfortunately comes at a cost due to the fact that the smaller the area we provide for convection, the larger the thermal resistance we will have between the TEG and the ambient.

In this work, we have adopted a theoretical model proposed by Teertstra *et al.* to estimate the thermal resistance of the parallel finned heat sinks used in our calculations.²² The model assumes forced convection as the main heat transfer mechanism but it also includes the impact of heat conduction through the fins. Using this model, it is possible for a given heat sink geometry and air velocity to calculate the Nusselt number, a value representing the ratio of heat transferred through convection off a surface *versus* conduction. This value can then be used to calculate the thermal resistance, $R_{HS} = 1/h_A A$ where A is the area of the TEG and h_A is the heat transfer coefficient of the heatsink measured in $\text{W m}^{-2} \text{ K}^{-1}$.

The calculated heat transfer coefficient of a small heat sink is plotted in Fig. 7 as a function of the thermal conductivity of the material used to construct the heat sink. The calculations were made assuming different air velocities ranging from almost zero to 1.4 m s^{-1} corresponding to walking at a normal pace.²³ The heat sink had 11 parallel fins, which were 0.5 mm thick and 5 mm tall. The base area of the heat sink was $1 \text{ cm} \times 1 \text{ cm}$.

There are several important conclusions we can draw from Fig. 7 for wearable thermoelectric harvesters. First, we can see that the heat transfer coefficient is a strong function of air velocity. This essentially implies that the performance of a wearable TEG will improve significantly if the person wearing the TEG is moving, which is consistent with experimental findings from researchers.^{3–5} For this reason, certain locations on the body (*e.g.* lower arm) are advantageous because they naturally move during tasks done by hands even if the person is not walking or running. Second, the impact of air velocity diminishes at higher velocities. This is somewhat disappointing because it implies that the TEG

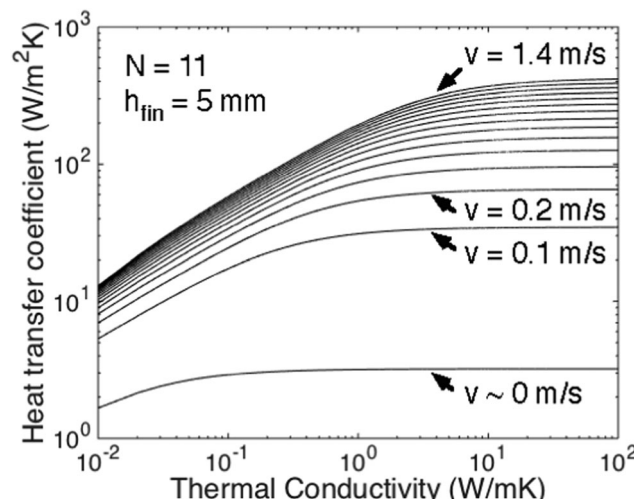


Fig. 7 Heat transfer coefficient of a small heat sink plotted as a function of the thermal conductivity of the heat sink material for different air velocities ranging from almost zero to 1.4 m s^{-1} often considered equivalent to normal walking pace.

performance will not improve significantly if the person moves even faster (*e.g.* running). Finally, we note that the heat transfer coefficient saturates beyond a certain thermal conductivity level and the saturation point shifts to higher values as the air velocity increases. Even more interestingly, we note that at $v = 1.4 \text{ m s}^{-1}$, there will not be anything gained from using a material with a thermal conductivity larger than $10 \text{ W m}^{-1} \text{ K}^{-1}$. This is significant because heat sinks are typically constructed of metals such as aluminum that are great thermal conductors. However, when the fin height is on the order of a few mm, the heat does not have to travel a large distance before it can leave the fins *via* convection. This observation opens the door to a variety of alternative materials including certain polymers with thermal conductivity levels above $5 \text{ W m}^{-1} \text{ K}^{-1}$ to create small, flexible heat sinks. In our calculations, we will assume a moderate heat sink with a heat transfer coefficient of $100 \text{ W m}^{-2} \text{ K}^{-1}$. This assumption also implies that a larger temperature drop will occur across the skin contact resistance with $h_c = 50 \text{ W m}^{-2} \text{ K}^{-1}$.

2.5 Material parameters

The model parameters used in this study (unless noted otherwise) are listed in Table 1. These parameters correspond to a semiconductor figure-of-merit zT , defined by:

$$zT = \frac{S^2 \sigma}{\kappa} T \quad (12)$$

of about $zT = 0.8$, typical of commercial TEGs based on the Bismuth Chalcogenide system. For simplicity, we have assumed that the parameters for p- and n-type legs are identical.

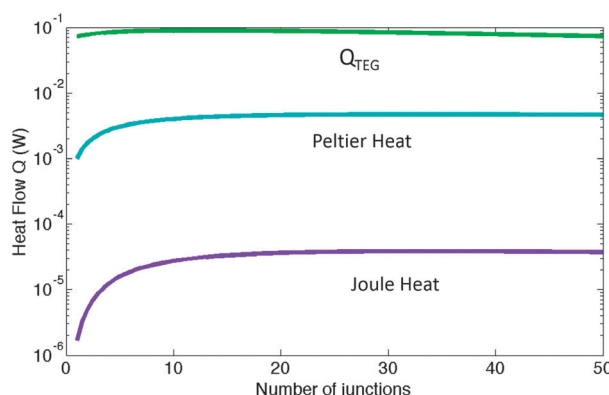
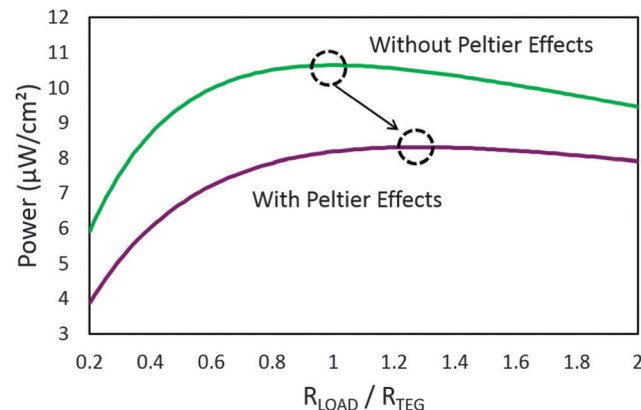
2.6 Optimum load resistance

According to the maximum power transfer theorem, the resistance of a load connected to a voltage source must match the output resistance of that source. If we assume this linear case,

Table 1 TEG parameters used in calculations

Parameter	Unit	Symbol	Value
Electrical conductivity	S cm^{-1}	σ	1000
Thermal conductivity	$\text{W m}^{-1} \text{K}^{-1}$	κ	1.5
Seebeck coefficient	$\mu\text{V K}^{-1}$	S	200
Electrical contact resistivity	$\Omega \text{ cm}^{-2}$	ρ_c	10^{-7}
Interconnect resistivity (Cu)	$\Omega \text{ cm}^{-2}$	$\rho_{\text{Cu}} u$	10^{-8}
Interconnect thickness	μm	h_{IC}	20
Substrate thermal conductivity	$\text{W m}^{-1} \text{K}^{-1}$	$\kappa_{\text{substrate}}$	200
Substrate thickness	mm	$h_{\text{substrate}}$	0.5
Leg height	mm	h_l	1
Leg base area	mm^2	A_l	0.25
Thermal conductivity of air	$\text{W m}^{-1} \text{K}^{-1}$	κ_{air}	0.025
Body heat transfer coefficient	$\text{W m}^{-2} \text{K}^{-1}$	h_B	50
Heatsink heat transfer coeff.	$\text{W m}^{-2} \text{K}^{-1}$	h_{HS}	100
TEG area	cm^2	A_{TEG}	1
Ambient temperature	$^{\circ}\text{C}$	T_{Ambient}	27
Skin temperature	$^{\circ}\text{C}$	T_{Body}	34

where $R_S = R_L$, then the max power can be defined as $P = V_{oc}^2 / 4R_L$. However, a TEG is a non-linear device, whose behavior is altered by Joule heating and Peltier heating/cooling as discussed in Section 2.1. Consequently, simple matching of the load and source resistances does not yield the optimum operation point. Fig. 8 illustrates the relative contributions of the Peltier heating/cooling as well as Joule heating to the total heat flowing through the module. It can be seen that the contribution of Joule heating is quite negligible, which is not surprising considering the magnitude of the electric current flowing through the module.⁵ On the other hand, the Peltier effect, while still small, can not be neglected. Fig. 9 shows the output power generated by the TEG as a function of the ratio of the external load resistance, R_{LOAD} to the TEG source resistance, R_{TEG} . Calculations were carried out both with and without including the Peltier effect. It can be seen that the Peltier effect results in a sizable drop in the output power. Furthermore, the maximum power is no longer reached when $R_{\text{LOAD}} = R_{\text{TEG}}$, but it is shifted to a larger value of $\approx 1.4R_{\text{TEG}}$. This value is consistent with the analytical expression $R_{\text{LOAD}} = R_{\text{TEG}}\sqrt{1 + ZT}$, which yields the optimum load resistance for a given ZT .^{5,24} We differentiate ZT (upper case) from zT (lower case) here to specify device ZT which is derived from the overall efficiency of

Fig. 8 Comparison of total heat flux flowing through the TEG, Q_{TEG} , vs. heat lost through Joule and Peltier effects.Fig. 9 Generated output power versus $R_{\text{LOAD}}/R_{\text{TEG}}$ ratio with and without Peltier effect.

the entire device versus material zT which is representative of a single leg.²⁵ Further calculations in this paper will include the Peltier effect as well as the load ratio of 1.4 corresponding to $ZT \approx 0.8$.

3 Results

Fig. 10 shows typical temperature distributions from the body's core to the ambient for both a warm (27°C) and cooler day (15°C). Since the body regulates heat (blood) flow as the ambient changes, varying skin temperatures for the two conditions must be taken into account. Skin temperatures of 34°C and 26.9°C for the forearm from Fig. 1 were correlated to the warm and cool ambient temperatures respectively. The calculations were carried out assuming a fill factor of 25%, which is about typical for commercial TEGs. It can be seen that only a small fraction of ΔT_e drops across the thermoelectric legs. While the ΔT across the TEG increased (from 0.5°C to 0.9°C) with

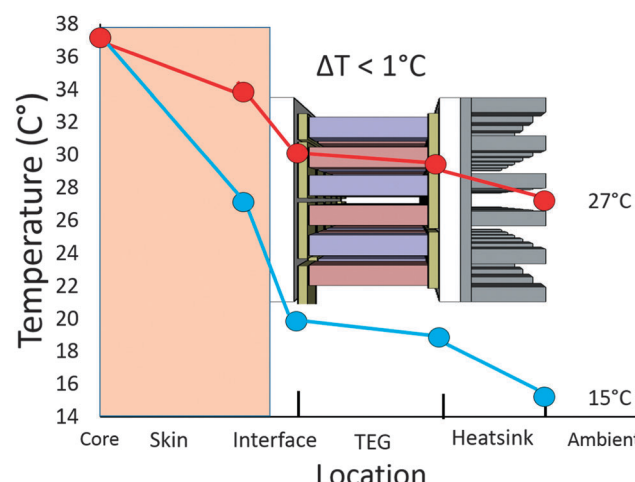


Fig. 10 Temperature difference from core body temperature to the ambient air. It can be seen that almost all of the temperature coming into the TEG is lost through the skin as well as the heatsink. Since the body regulates heat flow through the skin as function of the ambient, similar delta's across the TEG are obtained for varying ambient temperatures.

decreasing ambient temperature, the total percentage of available ΔT that falls across the TEG remained about the same around 4–5%. We can see from the figure that the skin resistance dominates over the TEG and heatsink thermal resistances. There is clearly not much that we can do to improve this except choose a location on the body that minimizes the skin resistance. The contact resistance will be helped by increasing the pressure but this may be a concern for long-term use. The heatsink resistance can be improved by increasing the fin area but again, this is not so desirable if the objective is to create a non-burdening device with a small form-factor. Ignoring the parasitic resistances, the module thermal resistance can be expressed as

$$R_{\text{TEG}} = \frac{1}{\kappa \text{FF} \times A_{\text{TEG}}} h_l \quad (13)$$

which leaves the semiconductor thermal conductivity, leg height, leg base-area and the fill factor (FF) as the four variables we can work with to improve the module performance. Fill factor is the percentage of total TEG area occupied by the thermoelectric legs. Another effect that needs to be considered is the heat conduction through the medium surrounding the legs, often referred to as the filler. Since the filler is effectively in parallel with R_{TEG} , it can have a substantial impact on the module resistance.

3.1 The effect of semiconductor thermal conductivity

Traditionally, research efforts in thermoelectric cooling and energy harvesting have emphasized material improvements to enhance the figure-of-merit, zT . It should be noted however that certain system requirements may increase the importance of certain parameters over others. Here, we show that body energy harvesting is one such application, for which, the thermal conductivity of the material is more important than the other two parameters (σ and κ) making up the zT .

Fig. 11 shows the output power against a varying thermal conductivity and Seebeck coefficient for two different zT s of 0.8 and 2.0 and two different cases of parasitic resistances. Fig. 11a considers a TEG with small source and heatsink thermal resistances. The calculations were performed assuming $h_A = h_B = 1000 \text{ W m}^{-2} \text{ K}^{-1}$. Using this heat transfer coefficient, the two parasitic resistances amount to a small percentage of the thermal resistance of the legs. On the other hand, Fig. 11b considers a TEG with much larger parasitic resistances typical for energy harvesting from the human body. Heat transfer coefficients of 100 and 50 $\text{W m}^{-2} \text{ K}^{-1}$ were assumed for h_A and h_B respectively.

The calculations were performed for a constant fill factor of 25%, leg length of 1 mm and base area of 0.25 mm^2 . To obtain the surface plots with constant zT values, the electrical conductivity was adjusted as κ and S were varied. Clearly, zT of 2.0 is hypothetical and it represents a value well beyond the reach of current commercial modules. While minimal, for a constant thermal conductivity, there does exist a slight increase in power with increasing Seebeck coefficient. We would not expect to observe this increase since the power factor, σS^2 , is kept constant as the electrical resistivity is tuned to keep the zT

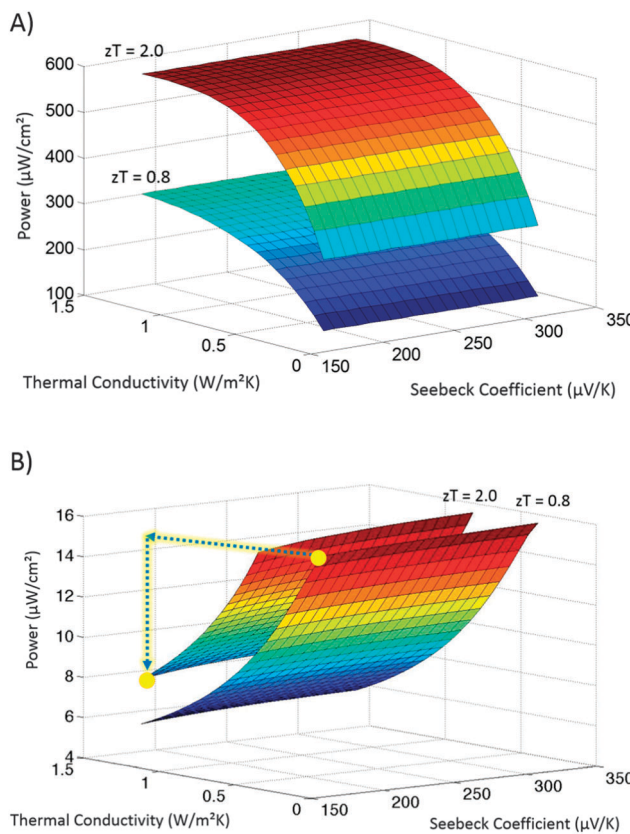


Fig. 11 Output power versus thermal conductivity and Seebeck coefficient for two different zT values. The calculations were performed for a constant fill factor of 25%, leg length of 1 mm and base area of 0.25 mm^2 . Thermal conductivity and Seebeck coefficient were varied and electrical conductivity was calculated to keep the overall zT constant (A) more common case of TEG with low input and output thermal resistances. (B) Wearable TEG with high input and output parasitic thermal resistances. It can be seen that for wearables, a TEG with a moderate zT of 0.8 but low thermal conductivity can outperform a TEG with a super high zT of 2.0 but higher thermal conductivity.

constant for each Seebeck coefficient. However, for a given zT and thermal conductivity, the increase in Seebeck coefficient corresponds to a decrease in electrical conductivity. As the electrical conductivity of the TE leg decreases, the current and therefore the secondary Peltier heating/cooling effects also reduce, yielding higher output power.

In Fig. 11a, we make two key observations. First, we can see that an improvement in zT always shows an improvement in performance for any permutations of Seebeck, thermal and electrical conductivity. Second, for either zT , as we lower the thermal conductivity for a given Seebeck coefficient, the output power decreases. This is because electrical conductivity must decrease with thermal conductivity to keep the zT constant. As such, lowering the thermal conductivity is equivalent to reducing the power factor, σS^2 and we can conclude that when the parasitic resistances are small, lowering the power factor results in a reduction of the output power.

On the other hand, the behavior in Fig. 11b is strikingly different. In this case, lowering the thermal conductivity

(hence the power factor) has the opposite effect of increasing the output power. Since the parasitic resistances are much larger than the resistance of the legs, only a fraction of the available temperature drops across the TEG. Given the fact that the output power is proportional to the square of ΔT_i , the impact of thermal conductivity on the output power is significant.

This interesting behavior brings up another observation about zT . The figure indicates that a material with $zT = 0.8$ and a very low thermal conductivity of $\kappa = 0.2 \text{ W m}^{-1} \text{ K}^{-1}$ can actually have twice the power of a system with $zT = 2.0$ and $\kappa = 1 \text{ W m}^{-1} \text{ K}^{-1}$. While we assert that zT is still important, we can see that lowering the thermal conductivity is far more critical than increasing the electrical conductivity (and hence, the power factor) for this particular application. This finding is consistent with the findings of Mayer *et al.* who noted the importance of κ over S and σ in heatsink limited applications.²⁶ This result shows potential promise for printable and flexible thermoelectrics for wearable applications, which exhibit low zTs but often have inherently very low thermal conductivities.^{27,28}

As a final note, we would like to emphasize that the above calculations and therefore conclusions were made for two materials with the same fill factor, leg height and base area. These parameters will clearly need to be optimized for a given thermal conductivity to achieve the best possible performance. These parameters are considered in more detail in the following section.

3.2 The effect of fill factor and physical dimensions

What dictates device performance is the thermal resistance of the module and how it compares to the parasitic resistances that exist in the overall system. In order to increase the module thermal resistance, we can reduce the fill factor, FF, by reducing the number of legs and/or decrease their base-area.

Fig. 12 compares the impact of changing the fill factor (number of legs) in three different TEGs, with semiconductor thermal conductivities of $\kappa = 0.2, 0.5$ and $1.5 \text{ W m}^{-1} \text{ K}^{-1}$. The legs are 1 mm tall and they have a base area of $0.5 \times 0.5 \text{ mm}^2$. The intrinsic temperature differential, ΔT_i , voltage and output power are plotted as a function of the number of legs (and FF).

Fig. 12a compares ΔT_i for the TEGs. As more legs are added, the TEG thermal resistance and the ΔT_i decreases. Not surprisingly, the module with the lowest thermal conductivity operates with a larger temperature differential throughout the entire FF range. For the most thermally conductive module, the temperature differential is less than 2°C once FF $> 10\%$. Fig. 12b compares the open-circuit voltages of the three TEGs. Clearly, the TEG with the lower thermal conductivity performs significantly better throughout the entire FF range. Finally, Fig. 12c shows that the TEG with $\kappa = 1.5 \text{ W m}^{-1} \text{ K}^{-1}$ reaches its maximum power at a very small fill factor (FF) of about 3% corresponding to about 10 legs. Increasing the fill factor causes a rapid drop in power resulting in a reduction of more than 50% at a fill factor of 20. On the other hand, with $\kappa = 0.2$, the maximum power is reached at FF ≈ 25 corresponding to ≈ 100 legs. It is important to note that it is quite challenging to construct a mechanically stable module with FF $< 20\%$ if the legs are attached using thermal compression bonding, as is the case now with commercial modules. Therefore, even though it is theoretically possible to reach about the same maximum power level with all three thermal conductivities, in practice, it will not be possible to produce a mechanically robust module with only a handful of legs. In conclusion, reducing the thermal conductivity allows us to construct modules with higher fill factors, which is needed for structural integrity.

Fig. 13 shows the device performance against different leg base areas, while keeping the leg height constant at 1 mm. The combination of both base area and the number of legs would therefore determine the fill factor for each curve. We can see that as we reduce the base area, the voltage increases for the same number of legs. On the other hand, the same output power is reached by all three devices but with different number of legs. While reducing the base area will increase the TEG resistance, the module's structural integrity will gradually worsen as we make the legs thinner and longer.

Finally, Fig. 14 explores the impact of leg height on TEG performance, while varying the fill factor but keeping the base area fixed at $0.5 \times 0.5 \text{ mm}^2$. Clearly, the performance steadily improves with increasing leg length. We can see that adjusting

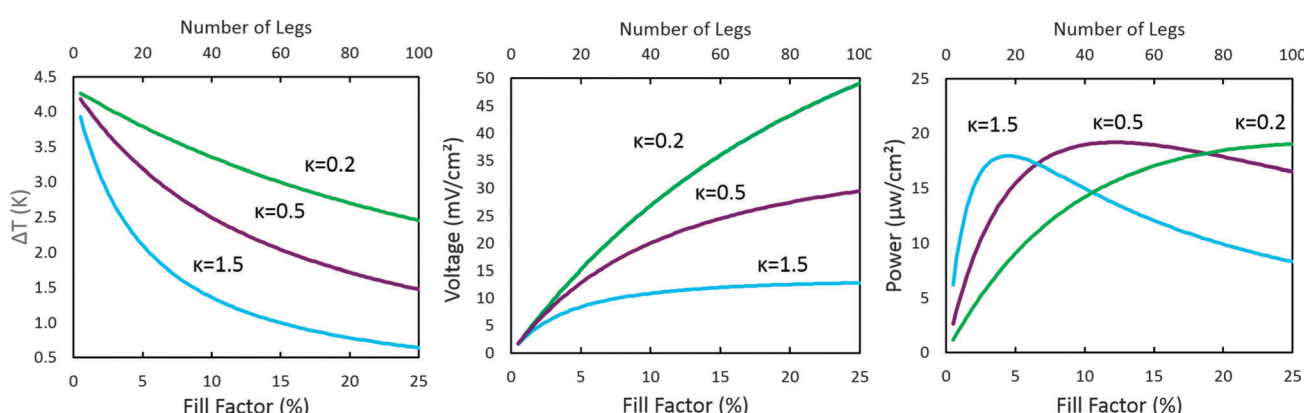


Fig. 12 Temperature differential, output voltage and output power for as a function of the fill factor for three different thermal conductivity values of $0.2, 0.5$ and $1.5 \text{ W m}^{-1} \text{ K}^{-1}$. Leg length was fixed at 1 mm, leg area at 0.025 mm^2 and TEG area at 1 cm^2 .

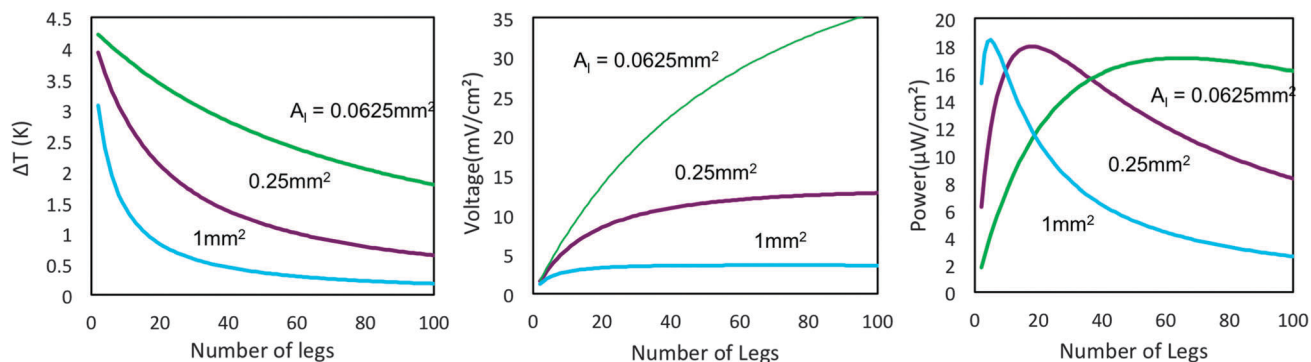


Fig. 13 Temperature differential across the TEG, output voltage and power as a function of leg count for varying leg base areas A_l . Leg length was fixed at 1 mm and TEG area at 1 cm^2 .

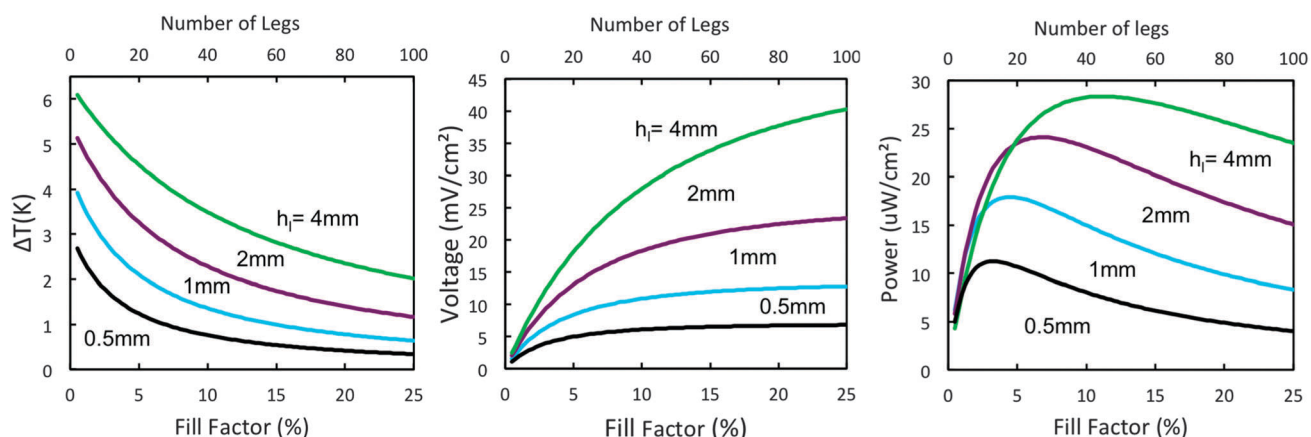


Fig. 14 Temperature differential across the TEG, output voltage and power for different leg lengths, h_l . Leg base area was fixed at 0.025 mm^2 and TEG area at 1 cm^2 .

the length also shifts the optimum operating point to slightly higher FFs. This finding is consistent with other researchers who have noted increased performance with leg length.^{5,29} Just as the case with base area, as we increase the leg length, we increase the leg thermal resistance which allows for a larger ΔT and increased voltage. However, as we increase the leg length, we also increase the distance for the heat to conduct through the filler material. It is this reduction of the filler thermal conductivity that allows for the overall increase in power in addition to the shift in FF, which is the subject of the next section.

Overall, geometry plays a crucial role in optimizing power output. The specific application where the TEG will be used will define the physical geometrical constraints and the TEG must be designed around those limitations. Leg length is the most dominant variable for increasing power, but it has been shown before that eventually, the electrical resistance starts to take over and decreases the overall power above a critical leg length.⁵ However these leg lengths are typically much too large for most wearable applications. If the maximum leg length is constrained by the application, then base area and thermal conductivity can be varied for optimization. Reducing the base area will increase the leg aspect ratio, which favorably increases the device thermal resistance. A smaller base area also allows for additional legs,

which can lead to a higher output voltage. However, there is a limit to the size of legs that can be cut using conventional saws. Material thermal conductivity can then provide a new degree of freedom in increasing the TEG resistance under both geometric and non-traditional constraints such as comfort and aesthetics for wearables.

3.3 The effect of filler thermal conductivity

In a typical TEG, air surrounds the semiconductor legs. While air has a fairly low thermal conductivity of $\kappa \approx 0.025 \text{ W m}^{-1} \text{ K}^{-1}$ at room temperature, its effect on TEG performance must be considered given the fact that 50% or more of the volume between the two substrates is filled with air. The impact of the filler material becomes even more critical if other materials are substituted for air. This is indeed the case for flexible TEGs, which typically use a polymer based material in place of air.

Fig. 15a shows the TEG output power density plotted as a function of the number of legs (or FF) for four different filler materials: vacuum, air, polydimethylsiloxane (PDMS), a popular elastomer commonly used as a flexible substrate material with $\kappa = 0.15 \text{ W m}^{-1} \text{ K}^{-1}$ and a theoretical case in which only half of the area is filled with PDMS resulting in composite air/PDMS thermal conductivity of $k = 0.08 \text{ W m}^{-1} \text{ K}^{-1}$. The base area for

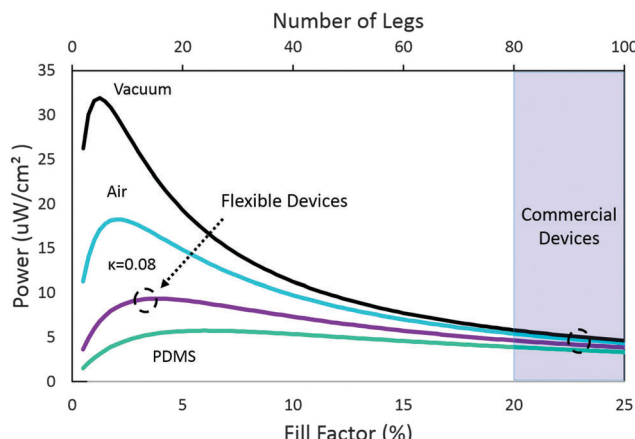


Fig. 15 Output power for four different filler materials: vacuum ($\kappa = \infty$), air ($\kappa = 0.025$), PDMS ($\kappa = 0.15$) and half air/PDMS ($\kappa = 0.08$) with an increased leg base area of $0.562 \mu\text{m}^2$. All powers converge to a similar power at fill factors above 20%. However, below 20%, flexible TEGs filled with PDMS perform comparably to air, and TEGs filled with a material with $\kappa = 0.08$ outperform commercial TEGs with only half of the number of leg couples.

these curves has been increased to $0.562 \mu\text{m}^2$ in order to have the maximum peaks more pronounced at lower fill factors. All four curves exhibit a similar behavior: a peak power is reached at a certain FF, which rapidly drops with increasing FF due to decreasing thermal resistance of the module as more legs are added. The peak power drops with increasing thermal conductivity of the filler material and it shifts slightly to larger FF values. At a first glance, it can be seen that this thermal shunting effect can have a significant impact on TEG performance. The maximum power drops from 31 to $17 \mu\text{W cm}^{-2}$, when the medium changes from vacuum to air. It then drops further with PDMS down to $5 \mu\text{W cm}^{-2}$. On the other hand, it is also evident that the impact of the medium becomes less dramatic at higher fill factors. All four curves converge to comparable power levels for $\text{FF} > 20\%$. For commercial TEGs, FF typically runs even higher in order to ensure the structural integrity of the module. It is interesting to note that for printable and flexible thermoelectrics, this point can actually be an advantage, since the mechanical restraint can be relaxed and lower FF can be realized. In this regime, we can see that a TEG with flexible filler materials can not only perform similar to that of air, but in the case of the half air/PDMS case, nearly double the performance of a standard TEG with a fill factor higher than 20%. Not only does this allow for the possibility of flexible TEGs outperforming their rigid counterparts, but the performance can be met at a reduction of more than half the amount of material needed, leading to a lower overall cost.

3.4 The effect of lateral heat flow and impact of substrates

A TEG relies on lateral flow of heat through the substrates to collect and reject heat effectively. On the hot-side, the heat collected from the entire area module area should move to the legs. Similarly, it is through this substrate that the rejected heat reaches the heatsink for convection. The thickness and the thermal conductivity of this substrate dictates the lateral thermal

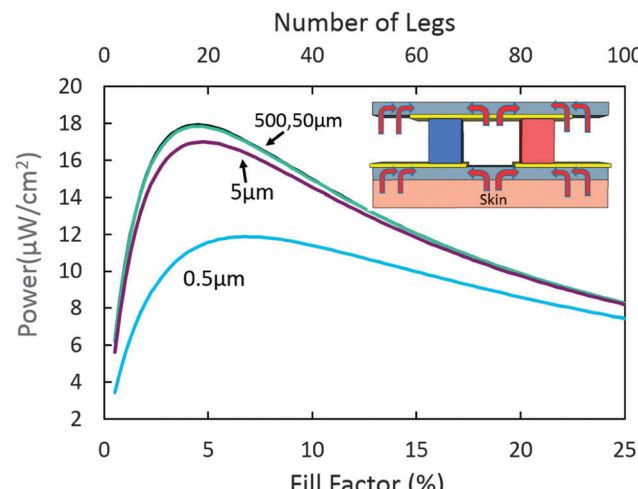


Fig. 16 Output power for different substrate thicknesses. It can be seen that above $5 \mu\text{m}$, substrate thickness does not effect the overall power. Thinner substrates for heat spreading can be advantageous for flexible TEGs, where metals need to be thin in order to maintain flexibility.

resistance included in our model with the resistors, R_{In} . In our calculations, we have assumed $\kappa = 200 \text{ W m}^{-1} \text{ K}^{-1}$ for the substrates. This value is close to the thermal conductivity of aluminum nitride ($\kappa \approx 185 \text{ W m}^{-1} \text{ K}^{-1}$ at 300 K) a commonly used substrate material for rigid TEGs. It is also close to the thermal conductivity of aluminum ($\kappa \approx 205 \text{ W m}^{-1} \text{ K}^{-1}$ at 300 K), which can serve as a thin heat spreader on flexible TEGs.

Fig. 16 shows the power plotted against the fill factor for different substrate thicknesses, decreasing from $500 \mu\text{m}$ – typical for a rigid TEG down to $0.5 \mu\text{m}$, which could be used to create a thin spreader on a flexible module. Air was assumed to be the medium surrounding the legs. It can be seen that the effect of the substrate thickness is small provided that the substrate thickness is above $5 \mu\text{m}$. Even at a thickness of $0.5 \mu\text{m}$, at high fill factors, the power levels are very similar to those obtained using thicker substrates. Therefore, flexible thermoelectrics that exploit a wearable form factor can still achieve sufficient heat spreading with thinner substrates or metal spreaders without sacrificing the overall performance.

3.5 Impact of external spreaders

Since wearable TEGs suffer from large thermal parasitic resistances, using heat spreaders that extend beyond the module area can be quite effective in enhancing the device performance. In these calculations, we have assumed that the spreader width is identical to that of the module and that the spreader extends the same length equally on either side of the TEG. We have assumed a $10 \mu\text{m}$ thick Cu spreader with a polymer cladding whose thickness is equal to the height of the TEG. The cladding was added to reduce the heat lost from the spreader to the ambient. Finally we assumed the same heat sink heat transfer coefficient, $h_{\text{HS}} = 100 \text{ W m}^{-2} \text{ K}^{-1}$ for the top of the cladding to the ambient. Lateral heat flow through the polymer cladding is assumed to be negligible and therefore only preferential through the Cu spreader. The external spreader was included in the model by a

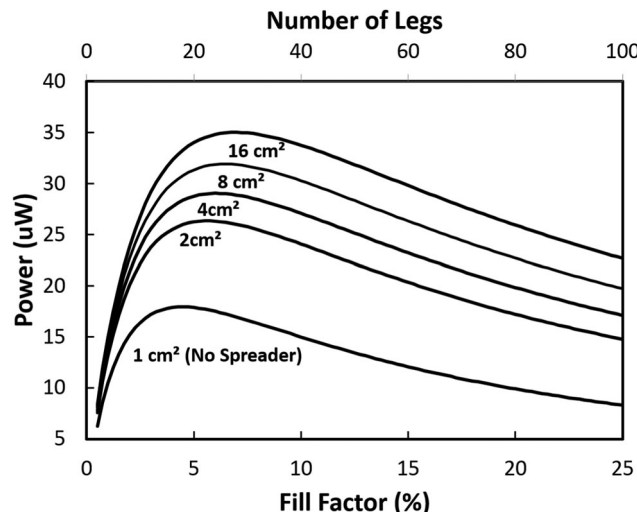


Fig. 17 Output power of a 1 cm^2 TEG with varying external spreader areas. It can be seen that significant improvement can be obtained by simply adding an external spreader to reduce the thermal resistance at the hot source.

resistor chain similar to that shown in Fig. 4a to calculate the lateral flow of heat around the legs, where R_v , R_{co} , R_l , and R_{ho} represent the vertical conduction through the polymer, the convective heat transfer to the ambient, lateral heat flow through the copper, and heat transfer through the skin respectively.

Shown in Fig. 17 is the output power plotted as a function of the leg count for a 1 cm^2 TEG with four different spreader areas. Also shown for comparison is the output power of a larger TEG with a surface area of 2 cm^2 but no spreader. It can be seen that the external spreader can make a significant contribution to the output power. However, this contribution decreases as the external spreader becomes too large compared to the TEG and the heat must travel a long distance. Clearly, the performance of the spreader will improve as the thickness of the spreader is increased to reduce the lateral thermal resistance. It is also important to note that this calculation also includes the heat loss to the ambient *via* conduction through the polymer on top of the spreader. This result is consistent with previous findings and can be improved with heat spreading on the cold side as well.⁴ For applications where space is in abundance, heat spreading might offer a way to provide large gain in performance, without any additional cost of thermoelectric modules and materials. For a wearable device such as a wristband, the heat spreader can be easily integrated into the band.

4 Experimental

In order to verify the potential impact that design optimizations could have on wearable TEGs a custom TEG was built and tested against a commercial off-the-shelf (COTS) TEG. Both TEGs used materials based on the Bismuth Chalcogenide system. The custom TEG used polycrystalline N type legs and nanostructured bulk p-type legs. Nanostructuring was employed in order to reduce the thermal conductivity of the material, which

Table 2 TEG parameters for both a custom TEG and COTS TEG. Leg parameters represent the average of n-type and p-type legs

Parameter	Custom	COTS
TEG area	0.97 cm^2	0.87 cm^2
Fill factor	28.3%	31.8%
Leg base area	0.36 mm^2	0.384 mm^2
Leg length	2.2 mm	1.2 mm
Leg Seebeck	$208\text{ }\mu\text{V K}^{-1}$	$210\text{ }\mu\text{V K}^{-1}$
Leg thermal conductivity	$1.14\text{ W m}^{-1}\text{ K}^{-1}$	$1.45\text{ W m}^{-1}\text{ K}^{-1}$
Leg electrical conductivity	807 S cm^{-1}	900 S cm^{-1}

was shown to be the most critical material parameter for wearable TEGs. n-Type legs had $S = 210\text{ }\mu\text{V K}^{-1}$, $\kappa = 1.5\text{ W m}^{-1}\text{ K}^{-1}$, $\sigma = 900\text{ S cm}^{-1}$ while the p-type legs exhibited $S = 206\text{ }\mu\text{V K}^{-1}$, $\kappa = 0.78\text{ W m}^{-1}\text{ K}^{-1}$, $\sigma = 715\text{ S cm}^{-1}$. Detailed description of the fabrication processes used to manufacture the nanostructured p-type legs as well as device integration will be published elsewhere.³⁰ The geometries of the legs were also optimized for higher performance on the human body by making the custom legs longer and thinner. The fill-factor of the custom and COTS TEGs were 28.3% and 31.8% respectively. A summary of the parameters is provided in Table 2. As discussed previously, the lower fill-factor also contributes to improved performance on the human body. To assemble the module, individual legs were bonded (using Indium 5.7LT solder) to Au coated Cu interconnects fabricated on an alumina substrate. A Finetech Fineplacer Pico thermocompression bonder was used at $200\text{ }^\circ\text{C}$ for 5 min with a force of 10 N. Table 2 summarizes the dimensions and material properties for the two devices. Fig. 18 shows the experimental setup used for testing the device as well as the images of the custom built TEG and a COTS module.

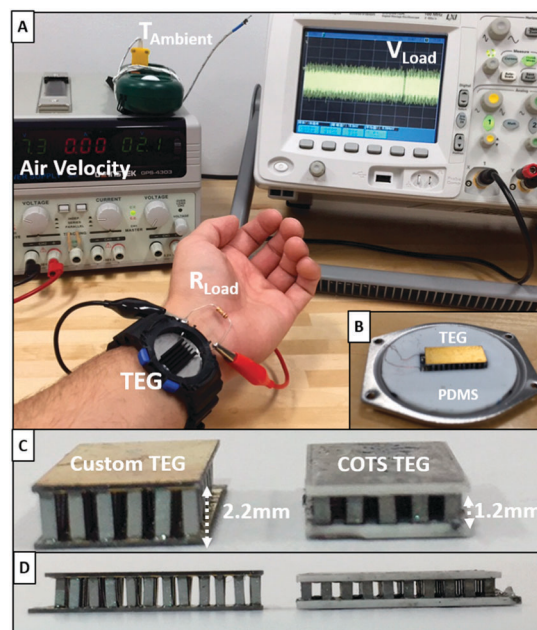


Fig. 18 (A) Experimental setup showing oscilloscope reading of load voltage and TEG wristband (with heatsink) on the wrist. (B) TEG fastened to the watch baseplate with PDMS thermal insulation. (C) Front view of the custom and COTS TEGs. (D) Side view of the custom and COTS TEGs.

Fig. 18a shows the experimental setup used for measuring the output voltages across a load from the TEGs. An Agilent DSO4012A 100 MHz Oscilloscope was used to record the output voltage from the TEG. A 12 VDC electric fan was used to cool the cold-side of the TEG via forced convection. A DC power supply was used to adjust the fan speed. The watch was placed on the wrist and held at a fixed distance of 20 cm. The voltage dependence of the air velocity was calibrated using an anemometer (extech 45170CM), which also recorded the ambient temperature. Load resistors were chosen for the optimal resistance as described by $R_{LOAD} = R_{TEG}\sqrt{1+ZT}$, where ZT was measured using a Z-meter (TEC DX4090). The load resistors for the custom and COTS TEGs were therefore chosen to be 9 and 1.9 ohms respectively. Fig. 18b shows the TEG placed inside of the baseplate of an empty watch case. This baseplate served as a 6 cm^2 spreader underneath the TEG. The TEG itself was centered and secured to the base plate using double sided carbon tape. A $10 \times 15 \times 4$ mm heatsink was also mounted to the device for some of the measurements using double sided carbon tape as well. The baseplate around the TEG was insulated using a thin PDMS layer in order to prevent active convective cooling by the fan. Fig. 18c shows a front view of the two TEGs, showing the leg width and length difference between the two. Fig. 18d shows a side view, showing the module showing again the geometry difference as well as slight difference in the fill factor.

Fig. 19 shows the average saturated output power for the two TEGs (without and without heatsinks) at air velocities of 0, 0.3, 0.6 and 0.9 m s^{-1} . Three individual measurements were made

for each air velocity for both the custom and COTS TEGs. All measurements at different air velocities for each respective TEG was made without removing it from the wrist. The order of air velocity measurements were also randomized. A thermal stabilization time of 5 min was allotted before each new measurement to allow for the TEGs to reach resting power levels. Once air flow was applied, output voltage across the load was recorded for 3 min. The average ambient temperature throughout all measurements was 22.6°C with a standard deviation of 0.4°C . In order to fit the model to the measured data, the body heat transfer coefficient h_B , and the heatsink heat transfer coefficient h_A need to be known. Because the skin temperature under the wrist watch is also an unknown, we have chosen to work with the known core body temperature of 37°C . Then, h_B includes the thermal resistance through the skin in addition to the contact resistance between the skin and watch baseplate, and heat transfer through the baseplate/carbon tape to the TEG. To determine the h_B without a heatsink, we assumed a heat transfer coefficient of $h_A = 5\text{ W m}^{-2}\text{ K}^{-1}$ for natural convection. This yielded $h_B = 15\text{ W m}^{-2}\text{ K}^{-1}$ for the COTS TEG, which very closely matches calculations discussed previously for the body and contact resistances in series in Section 2.3. Keeping h_B the same, h_A of 30, 35 and $40\text{ W m}^{-2}\text{ K}^{-1}$ for air velocities of 0.3, 0.6 and 0.9 m s^{-1} were found respectively.

The same calculations were repeated for the custom TEG using the same h_B and h_A values. However, it was determined that we needed to increase h_B from 15 to $18\text{ W m}^{-2}\text{ K}^{-1}$ to achieve a better match to the experimental data. This increase in h_B is suggestive of reduced skin resistance under the TEG, which can be attributed to a physiological change in the skin. This is expected in order to account for the increased thermal resistance to heat flow from the custom TEG. Since the custom TEG has a higher thermal resistance, the body has a harder time rejecting heat through the TEG. Therefore, blood flow through the skin would need to increase, lowering the skin resistance (*i.e.* increased h_B) allowing heat to flow easier.

The same procedure was followed for both devices after attaching a heatsink. The same h_B values of 15 and $18\text{ W m}^{-2}\text{ K}^{-1}$ were used for the COTS and custom TEGs respectively. The heat transfer coefficient, h_A was found to be 20, 100, 200 and $300\text{ W m}^{-2}\text{ K}^{-1}$ for air velocities of 0, 0.3, 0.6 and 0.9 m s^{-1} respectively.

As shown in Fig. 19, by properly designing the custom TEG, a $3\times$ improvement over the conventional COTS TEG is possible. It is important to note that further improvements will be possible by nanostructuring the n-type legs in the future. The power levels for both devices increase with increasing airflow but saturate above a certain level due to saturation of the heatsink thermal resistance according to $R_{HS} = 1/h_A A$. Furthermore, adding a heatsink provides an almost $4\times$ improvement by itself. It can be seen that the model predicts the performance improvements achieved by engineering the material properties, device design, and convection reasonably well. In our measurements, it was observed that the performance of both TEGs dropped the longer the wristbands were worn. This is the primary cause of the spread in the measured values. This suggests that a

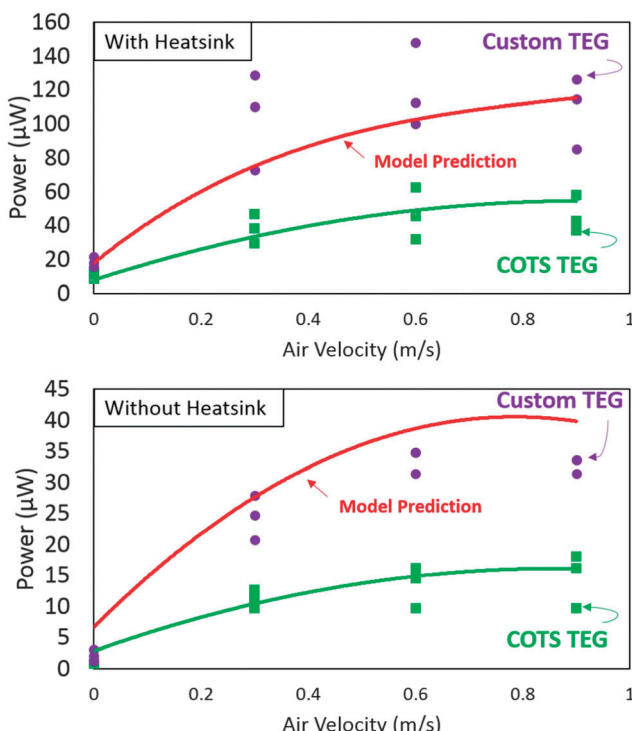


Fig. 19 Experimental comparison of custom and COTS TEG performance with and without heatsink using a 6 cm^2 heat spreader. The data points correspond to experimental data obtained from the wrist. The solid lines correspond to the model output.

stabilization time of 5 min was perhaps not long enough for the device to truly reach thermal equilibrium. It is also interesting to note that the spread is even larger with the heatsink because it is taking longer to reach thermal equilibrium conditions due to more effective convective cooling. Overall, we would like to emphasize that these are difficult measurements due to variations in contact resistance, ambient temperature as well as physiological changes in the skin. Nevertheless, the model predicts the overall experimental performance reasonably well thus providing a computationally efficient tool to optimize the TEG design for body energy harvesting.

Another viewpoint is to compare the power density in terms of the weight of the thermoelectric material used. The N and P type densities for the custom TEG were obtained from Archimedes measurements and were found to be 7.48 and 6.57 g cm⁻³ respectively. Theoretical densities of 7.69 and 6.72 g cm⁻³ for the N and P type legs were assumed for the COTs TEGs respectively. This yielded 0.39 grams of thermoelectric material used for the custom TEG and 0.17 grams for the COTs TEG. Model fit curves for the heatsink experimental data shown in Fig. 19 were used for comparisons. These calculations indicate that at rest, the custom and COTs TEGs produced 52 μW g⁻¹ and 46 μW g⁻¹, and with 0.9 m s⁻¹ air flow they produced 330 μW g⁻¹ and 325 μW g⁻¹ respectively. These numbers suggest that the COTS and custom TEGs are comparable when they are compared using power generated per unit weight. However, it is important to remember that these two TEGs have different leg lengths as shown in Fig. 18. To have a fair comparison, we simulated both power (μW) and power density (μW g⁻¹) for custom and COTS TEG materials as a function of leg length and the resulting curves are shown in Fig. 20. In these simulations, we have assumed the same dimensional parameters for both TEGs that belonged to the COTS TEG in Table 2. These calculations also assume $h_B = 15 \text{ W m}^{-2} \text{ K}^{-1}$, $h_A = 300 \text{ W m}^{-2} \text{ K}^{-1}$ and a 6 cm² spreader.

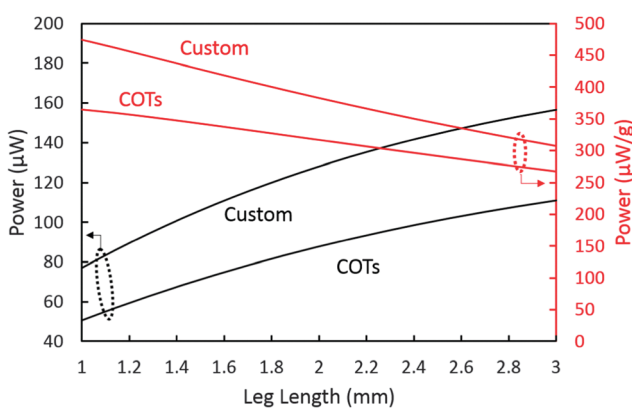


Fig. 20 Simulated comparison of a TEG using custom and COTS materials versus varying leg length. The calculations were performed using the same dimensional parameters as the experimental COTS TEG including a TEG area of 0.87 cm², leg base area of 0.384 mm², number of legs = 50 and a 6 cm² spreader. An air velocity of 0.9 m s⁻¹ was also assumed for the calculations. It can be seen that the material enhancement in the custom legs, most notably the reduction in thermal conductivity, causes an improvement in both power and power density over all leg lengths.

It can be seen that the custom TEG yields more power as well as more power density at any leg length. Both of these improvements can be attributed to enhancements in material properties, most notably the thermal conductivity. However, It is interesting to note that for both TEGs, the power density is decreasing with increasing length. This is due to the fact that the power starts to saturate as we increase the leg length due to increasing electrical resistance. Therefore as we add more material, we are not gaining as much in power causing a reduction in power density.

5 Conclusions

Designing thermoelectric modules for energy harvesting on the human body pauses unique challenges. Current commercial TEGs only experience around 1 °C drop of temperature across the TEG itself even though the body to ambient temperature can be as large as 10 °C or more. The majority of this temperature differential drops across the skin itself and the parasitic thermal resistances at the skin/TEG and TEG/ambient interfaces. This small temperature differential severely limits the energy that can be harvested from the body resulting in power levels on the order of tens of microwatts per cm². Maximizing the temperature differential across the TEG legs requires increasing the thermal resistance of the semiconductor legs while minimizing all thermal parasitic resistances. In this work, we have developed a computationally efficient, quasi 3-D model to study the impact of all critical design parameters on the performance of body wearable TEGs. Our results indicate that successful use of TEGs in body energy harvesting requires a multi-prong approach, which includes a good module design to reduce the parasitic losses as well as improvements in material properties optimized for the application. We assert that while zT is important, the critical parameter for body-wearable TEGs is the thermal conductivity of the semiconductor material. Our results indicate that a good module design must carefully consider the impact of the semiconductor properties as well as second order effects such as heat conduction through the filler material and two-dimensional spreading of heat in the headers – especially for flexible devices with thinner conducting materials. External heat spreaders can also help significantly by increasing the area for heat collection. Without any additional thermoelectric material, these spreaders alone can double the performance of a wearable TEG. For flexible TEGs, the critical parameters include the thermal conductivity of the filler material, fill factor and spreading of the heat between the legs through thin, flexible conductors. With these parameters taken into consideration, it is possible for a flexible TEG to be designed such that it would out perform its rigid counterparts. Finally, the model was used to optimize the material properties and device design to construct a custom TEG using nanocomposite p-type and standard polycrystalline n-type BiTe legs. The results indicate that it is possible to design a TEG system that can provide 20 μW continuously with no air flow. Given the fact that more TEGs can be placed on a wearable band, it should be possible to harvest significantly

more power even when the person is at rest. With air flow (*i.e.* motion), the custom TEG output power jumps to 120 µW suggesting that with an optimal heat spreader and more TEGs, the harvested power can approach mW.

Acknowledgements

This work was supported by the Advanced Self-Powered Systems of Integrated Sensors and Technologies (ASSIST), a Nano-Systems Engineering Research Center funded by National Science Foundation (EEC1160483). Daryoosh Vashaee acknowledges the funding support by Air Force Office of Scientific Research grant FA9550-12-1-0225 and NSF grants ECCS-1351533 and CMMI-1363485. The authors would like to thank Allen Gray, Robert Therrien, Art Prejs, Patrick Wellenius and Wael Shyukhi at Phononic for their help with thermocompression bonding. Special thanks from Mehmet C. Ozturk go to his friend, Raif O. Onvural for inspiring him to start his work in thermoelectrics.

References

- 1 M. Kishi, H. Nemoto, T. Hamao, M. Yamamoto, S. Sudou, M. Mandai and S. Yamamoto, *Eighteenth International Conference on Thermoelectrics*, 1999, pp. 301–307.
- 2 V. Leonov, P. Fiorini, S. Sedky, T. Torfs and C. Van Hoof, Solid-State Sensors, Actuators and Microsystems, 2005. Digest of Technical Papers. TRANSDUCERS'05. The 13th International Conference on, 2005, pp. 291–294.
- 3 V. Leonov, T. Torfs, P. Fiorini and C. Van Hoof, *IEEE Sens. J.*, 2007, **7**, 650–657.
- 4 K. T. Settaluri, H. Lo and R. J. Ram, *J. Electron. Mater.*, 2012, **41**, 984–988.
- 5 M. Lossec, B. Multon, H. Ben Ahmed and C. Goupil, *Eur. Phys. J.: Appl. Phys.*, 2010, **52**, 11103.
- 6 J.-H. Bahk, H. Fang, K. Yazawa and A. Shakouri, *J. Mater. Chem. C*, 2015, **3**, 10362–10374.
- 7 Y. Zhang, F. Zhang, Y. Shakhsheer, J. Silver, A. Klinefelter, M. Nagaraju, J. Boley, J. Pandey, A. Shrivastava, E. Carlson, A. Wood, B. Calhoun and B. Otis, *IEEE J. Solid-State Circuits*, 2013, **48**, 199–213.
- 8 T. Torfs, V. Leonov, C. Van Hoof and B. Gyselinckx, *Sensors, 2006. 5th IEEE Conference on*, 2006, pp. 427–430.
- 9 V. Misra, A. Bozkurt, B. Calhoun, T. Jackson, J. Jur, J. Lach, B. Lee, J. Muth, O. Oralkan, M. Ozturk, S. Trolier-McKinstry, D. Vashaee, D. Wentzloff and Y. Zhu, *Proc. IEEE*, 2015, **103**, 665–681.
- 10 J. A. Harris and F. G. Benedict, *Proc. Natl. Acad. Sci. U. S. A.*, 1918, **4**, 370.
- 11 A. Burton, *Am. J. Physiol.*, 1939, **127**, 437–453.
- 12 C. Huizenga, Z. Hui and E. Arens, *Building and Environment*, 2001, **36**, 691–699.
- 13 P. Webb, *Eur. J. Appl. Physiol. Occup. Physiol.*, 1992, **64**, 471–476.
- 14 R. L. Boylestad, *Introductory Circuit Analysis*, Prentice Hall, 2010.
- 15 M. Yovanovich, J. Culham and P. Teertstra, *Electronics Cooling*, 1997, **3**, 24–29.
- 16 H.-N. Ho and L. Jones, *et al.*, *Haptic Interfaces for Virtual Environment and Teleoperator Systems Symposium on*, 2006, pp. 461–467.
- 17 Y. Mori, E. Kioka and H. Tokura, *Int. J. Biometeorol.*, 2002, **47**, 1–5.
- 18 L. Tchvialeva, H. Zeng, I. Markhvida, D. I. McLean, H. Lui and T. K. Lee, *New Developments in Biomedical Engineering*, InTech, 2010, pp. 341–358.
- 19 Y. Kurazumi, T. Tsuchikawa, J. Ishii, K. Fukagawa, Y. Yamato and N. Matsubara, *Building and Environment*, 2008, **43**, 2142–2153.
- 20 J. Sarabia, M. Rol, P. Mendiola and J. Madrid, *Physiol. Behav.*, 2008, **95**, 570–580.
- 21 R. J. de Dear, E. Arens, Z. Hui and M. Oguro, *Int. J. Biometeorol.*, 1997, **40**, 141–156.
- 22 P. Teertstra, M. Yovanovich and J. Culham, *J. Electron. Manuf.*, 2000, **10**, 253–261.
- 23 K. Fitzpatrick, M. Brewer and S. Turner, *Transp. Res. Rec.*, 2006, 21–29.
- 24 A. Montecucco, J. Siviter and A. R. Knox, *Appl. Energy*, 2015, **149**, 248–258.
- 25 G. J. Snyder and E. S. Toberer, *Nat. Mater.*, 2008, **7**, 105–114.
- 26 P. Mayer and R. Ram, *Nanoscale Microscale Thermophys. Eng.*, 2006, **10**, 143–155.
- 27 O. Bubnova, Z. U. Khan, A. Malti, S. Braun, M. Fahlman, M. Berggren and X. Crispin, *Nat. Mater.*, 2011, **10**, 429–433.
- 28 G. Kim, L. Shao, K. Zhang and K. P. Pipe, *Nat. Mater.*, 2013, **12**, 719–723.
- 29 M. Gomez, R. Reid, B. Ohara and H. Lee, *J. Appl. Phys.*, 2013, **113**, 174908.
- 30 A. Nozariasbmarz, F. Suarez, J. Dycus, M. Cabral, M. Ozturk and D. Vashaee, 2016, to be published.